PAPER

Check for updates

BiFe$_{0.5}$Cr$_{0.5}$O$_3$ nanocatalysts for sustainable solar-light-driven purification of pharmaceutical wastewater†

Titas Vincent Rozario, Mohasin Tarek [ID] and M. A. Basith [ID] *

Pharmaceutical wastewater contamination, particularly from antibiotics, poses severe environmental and health risks due to antibiotic-resistant bacteria and the inefficacy of conventional treatments. In this study, BiFe$_{0.5}$Cr$_{0.5}$O$_3$ (BFCO) nanoparticles were synthesized *via* the sol–gel method and investigated as a visible-light-driven photocatalyst for ciprofloxacin (CIP) and levofloxacin (LFX) degradation under solar irradiation. The structural analysis confirmed a single-phase perovskite structure with Cr^{3+} incorporation, enhancing charge separation and visible-light absorption. The presence of oxygen vacancies, identified through XPS and Raman spectroscopy, played a crucial role in charge transfer and reactive oxygen species (ROS) generation. Comprehensive electrochemical and photoelectrochemical analyses, including CV, LSV, and EIS, confirmed enhanced charge transport and reduced interfacial resistance under illumination. BFCO, with a bandgap of 1.87 eV, exhibited efficient solar energy utilization, achieving 70.35% CIP and 94% LFX degradation within 240 minutes, following pseudo-first-order kinetics. The activation energy decreased from 33.61 ± 5.88 to 19.69 ± 3.94 kJ mol^{-1} K^{-1}, confirming enhanced catalytic efficiency. An apparent quantum yield (AQY) of 34.9% for LFX further underscored its superior activity. Scavenger studies identified electron (e$^-$) and superoxide ($^{\bullet}$O$_2^-$) radicals as key ROS driving antibiotic degradation, while oxygen vacancies improved charge separation and ROS formation. Reusability tests confirmed BFCO's stability across multiple cycles, maintaining its structural, morphological, and optical integrity. The degradation mechanism involves solar-induced electron–hole pair generation, charge transfer to oxygen vacancies, and subsequent redox reactions that break down antibiotics into non-toxic byproducts. The synergistic effects of Cr substitution, oxygen vacancies, and mixed-valence states significantly enhanced photocatalytic efficiency, demonstrating BFCO's potential for large-scale environmental remediation.

1 Introduction

Pharmaceutical wastewater from antibiotic production, hospitals, and improper medicine disposal has become a significant environmental concern.[1] Antibiotics such as ciprofloxacin, tetracycline, amoxicillin, and sulfamethoxazole persist in water bodies, promoting the emergence of antibiotic-resistant bacteria and genes, which pose severe risks to public health.[2–4] Furthermore, their resistance to natural degradation makes removal particularly challenging, and conventional wastewater treatment methods often fail to eliminate them effectively.[1–4]

Nanotechnology Research Laboratory, Department of Physics, Bangladesh University of Engineering and Technology, Dhaka, 1000, Bangladesh. E-mail: mabasith@phy.buet.ac.bd

In response to this challenge, conventional wastewater treatment plants (WWTPs) employ a combination of physical, chemical, and biological processes to reduce contaminants.[5–9] Screening and sedimentation remove large debris, while coagulation and flocculation help eliminate suspended and dissolved matter.[7,9] Additionally, biological treatment relies on microorganisms to break down organic pollutants, and disinfection through chlorination or UV irradiation eliminates pathogens.[8] Despite these efforts, antibiotics' complex chemical structures and low concentrations in wastewater make them highly resistant to degradation.[10] Moreover, some antibiotics can transform into metabolites that may be equally or more toxic than the original compounds, further complicating their removal.[10,11]

Given these limitations, there is an urgent need for more efficient and sustainable treatment methods. One promising solution is solar-driven photocatalysis, which leverages semiconductor materials and sunlight to generate reactive species capable of breaking down antibiotics into harmless byproducts.[12–14] Unlike conventional methods, this approach

ensures complete mineralization, eliminating the formation of toxic intermediates. Furthermore, it reduces dependence on fossil fuels, minimizes hazardous waste, and provides an environmentally friendly alternative for pharmaceutical wastewater treatment.[15] As a result, solar-driven photocatalysis presents a highly effective and sustainable strategy for addressing the growing issue of antibiotic contamination in water bodies.[15]

In recent years, semiconductor materials such as titanium dioxide (TiO_2),[16] zinc oxide (ZnO),[17] and cadmium sulfide (CdS)[18] have been extensively investigated for photocatalytic wastewater treatment due to their potential for environmental remediation. TiO_2 is particularly favored for its chemical stability, non-toxicity, and cost-effectiveness. However, its wide bandgap energy of 3.2 eV restricts its photoresponse to the ultraviolet (UV) region, limiting its efficiency under visible light.[16,19] Similarly, ZnO exhibits comparable photocatalytic behavior and bandgap characteristics but suffers from intrinsic drawbacks such as photo-corrosion and limited visible-light absorption.[20] In contrast, CdS possesses a narrower bandgap, enabling effective utilization of visible light.[21] Nonetheless, its practical application is hindered by issues of toxicity and poor photostability due to rapid photo corrosion.[22,23]

A common limitation across these traditional photocatalysts is the high recombination rate of photoinduced electron–hole pairs, which significantly reduces the overall photocatalytic efficiency. To overcome these drawbacks, recent research has shifted toward the development of heterostructured photocatalysts and photocatalytic fuel cells (PFCs) that operate effectively under visible light. For instance, advanced systems such as $NiFe_2O_4/Bi_2WO_6$/ZnO nanorods and Fe_2WO_6/ZnO photoanodes have demonstrated simultaneous degradation of antibiotics and energy generation *via* S-scheme heterojunction.[24,25] Likewise, Eu-doped BiOBr and Fe_2WO_6/Eu-BiOBr composites have shown efficient removal of organic pollutants and Cr(VI), attributed to enhanced charge separation and reactive species generation.[26,27] Additionally, pine tree-like $NiFe_2O_4$/ZnO photoanodes have exhibited strong photocatalytic activity along with antibacterial effects against industrial pollutants.[28]

While these hybrid systems demonstrate excellent performance, their complexity poses challenges for scalability and stability. Consequently, recent attention has turned to developing single-component photocatalysts with visible-light activity, improved charge carrier dynamics, and structural robustness. Among the promising alternatives, perovskite oxides, particularly bismuth ferrite ($BiFeO_3$), have garnered attention due to their unique crystal structure and tunable electronic properties.[29,30] $BiFeO_3$ (BFO) has several advantageous features, such as ferroelectric and antiferromagnetic properties, which could enhance photocatalytic activity.[31–33] Moreover, the perovskite structure allows the incorporation of various metal ions, facilitating the modification of the material's optical and electronic properties.[34] This versatility has made BFO a promising candidate for photocatalytic degradation of organic pollutants under visible light, making it suitable for solar-driven applications.[35,36]

However, despite its promise, BFO suffers from several inherent limitations that hinder its photocatalytic performance.

The primary challenges include high electron–hole recombination, low electrical conductivity, and non-optimal band edge positions for efficient redox reactions.[37,38] These limitations reduce its overall photocatalytic efficiency. Furthermore, $BiFeO_3$ nanoparticles tend to agglomerate, leading to a decrease in their active surface area, which is critical for effective photocatalysis.[37,38] Additionally, the potential leaching of Bi^{3+} ions from the material raises environmental concerns, as these ions can pose toxicity risks.[39] These challenges necessitate the development of strategies to enhance the photocatalytic efficiency, stability, and environmental safety of BFO.

To overcome these limitations, various modification strategies have been explored. These include cation doping,[34] oxygen vacancy engineering,[40] heterostructure formation.[41] Among these, Fe-site substitution with Er, Sn, Se, Ni, Mn and Cr metal ions has proven to be effective in enhancing charge separation, modifying the band structure, and improving charge mobility.[42–48]

Among the various substituent options, chromium (Cr) stands out as one of the most promising approaches for enhancing the photocatalytic performance of BFO.[49,50] The substitution of Fe with Cr^{3+} ions modifies the electronic band structure, leading to improved visible-light absorption and enhanced charge mobility. Additionally, this substituting reduces the electron–hole recombination rate, a major factor limiting photocatalytic efficiency in BFO. Cr^{3+} substitution shifts the conduction band downward, facilitating the formation of reactive superoxide radicals, while the valence band position remains suitable for hydroxyl radical ($^\bullet$OH) generation. These modifications result in better charge separation, higher charge carrier density, and increased surface reactivity, which collectively enhance photocatalytic activity. Consequently, $BiFe_{0.5}Cr_{0.5}O_3$ (BFCO) emerges as a superior photocatalyst for wastewater treatment, particularly in the degradation of pharmaceutical contaminants such as ciprofloxacin (CIP) and levofloxacin (LFX).

In addition to the benefits of Cr substitution, the introduction of oxygen vacancies in the BFCO structure further improves its photocatalytic performance.[40] Oxygen vacancies play a crucial role in enhancing charge transport by acting as trapping sites for charge carriers, which accelerates electron transfer processes.[51,52] The presence of oxygen vacancies also increases the availability of reactive sites on the catalyst surface, promoting the generation of reactive oxygen species that are vital for breaking down organic pollutants. As a result, the BFCO exhibits superior photocatalytic efficiency, with faster degradation rates and more efficient pollutant removal under visible light. Furthermore, the incorporation of oxygen vacancies enhances the material's stability, preventing Bi^{3+} leaching and ensuring that the catalyst remains durable over multiple photocatalytic cycles. This stability, coupled with faster electron transfer, makes BFCO an ideal candidate for long-term, cost-effective, and sustainable photocatalytic applications.

Another significant advantage of BFCO is its structural stability. Cr substitution not only improves photocatalytic performance but also contributes to maintaining the integrity of the material during photocatalytic reactions. This stability is

essential for the catalyst's reusability, as it ensures that the material does not degrade over time.[49,50] Furthermore, the presence of Cr influences the surface morphology, increasing the number of active sites available for photocatalytic reactions. In addition, the mixed metal oxide structure of BFCO provides synergistic effects that further enhance its photocatalytic performance. The combination of Bi and Cr elements in the perovskite structure leads to a unique electronic environment that promotes efficient charge separation and increases the overall photocatalytic efficiency.

To fully assess the photocatalytic performance of BFCO, several key analyses must be conducted. First, efficient catalyst recovery after treatment is essential for reusability, which can be achieved through various separation techniques, such as filtration, centrifugation, or magnetic separation.[34] Furthermore, determining the apparent quantum yield of the photocatalytic system provides valuable information regarding the efficiency of light utilization and the overall performance of the system.[51–53] This involves quantifying the number of antibiotic molecules degraded per photon absorbed by the catalyst, offering insights into the catalyst's light absorption efficiency. In addition, understanding the catalyst's band edge positions is critical for optimizing the charge transfer mechanism and reactive oxygen species (ROS) generation, which are key for enhancing photocatalytic performance.[51–53] Calculating the activation energy provides further insights into the kinetics of the degradation reaction and the impact of temperature on the process. Finally, rigorous reusability tests involving repeated cycles of photocatalytic degradation and catalyst recovery, are essential for assessing the long-term performance, stability, and economic viability of the catalyst for practical wastewater treatment applications.[51–53]

In this context, our study introduces BFCO nanoparticles synthesized *via* a sol–gel method as a novel, efficient, and reusable photocatalyst for the solar-light-driven degradation of pharmaceutical contaminants. The originality of this work lies in the strategic Cr^{3+} substitution at the Fe-site of BFO, which, in synergy with engineered oxygen vacancies and mixed-valence states, significantly enhances charge separation, lowers activation energy, and promotes reactive oxygen species (ROS) generation under solar light. Unlike previously reported BFO-based systems, the BFCO catalyst demonstrates superior photocatalytic performance, achieving high degradation efficiencies for both CIP and LFX, along with excellent apparent quantum yield and reusability over multiple cycles. These results represent an important scientific advancement toward the development of stable and cost-effective nanocatalysts for sustainable pharmaceutical wastewater remediation under solar irradiation.

2 Materials preparation and experimental techniques

2.1 Materials

In this investigation, the following analytical grade reagents were used for materials synthesis: $Bi(NO_3)_3 \cdot 5H_2O$ (Sigma-Aldrich, 99.80%), $Fe(NO_3)_3 \cdot 9H_2O$ (Sigma-Aldrich, 98.00%), $Cr(NO_3)_3 \cdot 9H_2O$ (Sigma-Aldrich, 98.00%), citric acid ($C_6H_8O_7$), NH_4OH, ethylene glycol CH_2OHCH_2OH, ciprofloxacin, levofloxacin, $AgNO_3$, ethylenediaminetetraacetic acid disodium salt (EDTA–2Na), benzoquinone(p-BQ), *tert*-butyl alcohol (t-BuOH), Na_2SO_4, N-methyl-2-pyrrolidone [C_5H_9NO] and poly(vinylidene fluoride) [$CH_2CF_2)_n$]. All chemicals purchased from Sigma-Aldrich, Germany, were used without any further purification.

2.2 Synthesis and characterization techniques

2.2.1 Synthesis of BFCO nanoparticles.
BFCO nanoparticles were synthesized using a sol–gel technique,[34,52–54] as illustrated in Fig. S1,† with detailed synthesis methods provided in the ESI.†

2.2.2 Characterization techniques.
The structural, morphological, elemental, and optical characteristics of the synthesized BFCO nanoparticles were systematically analyzed using multiple techniques. X-ray diffraction (XRD) was employed to determine the crystal structure, using a Rigaku SmartLab diffractometer equipped with copper K-alpha radiation. Surface morphology was examined *via* Field Emission Scanning Electron Microscopy (FESEM) with a GeminiSEM 360 (Zeiss, Germany) and Transmission Electron Microscopy (TEM) using a Talos F200X (Thermo Fisher Scientific, USA). The elemental composition was confirmed through Energy Dispersive X-ray (EDX) spectroscopy. Additionally, X-ray Photoelectron Spectroscopy (XPS) (Thermo Fisher Scientific, USA) was performed to investigate the chemical states and binding energies of constituent elements. The optical properties were analyzed using a UV-visible spectrophotometer (UV-2600, Shimadzu, Japan) and Photoluminescence Spectroscopy (PL) (RF-6000, Shimadzu, Japan). Electrochemical characteristics were examined using an Autolab PGSTAT302N electrochemical workstation (Metrohm, Germany).

2.2.3 Electrochemical and photoelectrochemical characterization techniques.
The electrochemical and photoelectrochemical[52,53] setup and methodology are detailed in the ESI (Fig. S2†).

2.2.4 Photocatalytic characterization techniques.
The photocatalytic performance of BFCO nanoparticles was assessed for the degradation of CIP and LFX under simulated solar irradiation. A 500 W Hg–Xe lamp with an irradiation power density of 100 mW cm^{-2} served as the light source. The experimental setup is schematically represented in ESI Fig. S3.† For the degradation experiments, 1 mg of CIP or LFX was dissolved in 100 mL of distilled water, and its absorbance spectrum was recorded using a UV-visible spectrophotometer (UV-2600, Shimadzu, Japan). A 20 mg portion of the BFCO nanoparticles was dispersed in 50 mL of the prepared CIP solution. The suspension was stirred in the dark for one hour to ensure adsorption–desorption equilibrium before initiating photocatalysis. Upon exposure to irradiation, aliquots of 5 mL were extracted at 30 minute intervals, centrifuged at 6000 rpm for 2 minutes, and analyzed using UV-visible spectrophotometry to determine the residual pollutants concentration. This

procedure was continued for up to 4 hours. The UV-Vis absorbance of CIP and LFX was monitored at their respective maximum absorbance wavelengths of 285 nm and 290 nm, respectively.

Active species trapping experiments were conducted to identify key reactive species responsible for the photocatalytic degradation. Specific scavengers were used: $AgNO_3$ for electrons (e^-), ethylenediaminetetraacetic acid disodium salt (EDTA-2Na) for holes (h^+), benzoquinone (p-BQ) for superoxide radicals ($^\bullet O_2^-$) and tert-butyl alcohol (t-BuOH) for hydroxyl radicals ($^\bullet OH$). Each scavenger was introduced at a concentration of 1.5 mM, and the degradation efficiency was evaluated based on the suppression of pollutant removal.

To determine the activation energy of the photocatalytic reaction, an LFX solution (1 mg in 100 mL distilled water) was prepared, and BFCO nanoparticles (20 mg and 40 mg) were separately dispersed in 50 mL of the solution. After achieving adsorption–desorption equilibrium in the dark for one hour, the mixture was irradiated under a solar simulator. Absorbance spectra were recorded at 30 minute intervals at different temperatures (25, 40, and 60 °C) to assess the temperature dependence of the photocatalytic degradation process.

3 Results and discussion

3.1 Structural, morphological, magnetic, optical, photoelectrochemical and chemical states analyses

The XRD spectrum of $BiFe_{0.5}Cr_{0.5}O_3$ nanoparticles, shown in Fig. 1(a), confirms a single-phase rhombohedral distorted perovskite structure with an $R3c$ space group.[55–57] Specifically, the XRD pattern of the synthesized BFCO nanoparticles closely aligns with the standard diffraction data of rhombohedral BFO, as referenced by JCPDS card no. 71-2494.[58] The absence of secondary phases such as $Bi_2Fe_4O_9$ or $Bi_{25}FeO_{40}$ indicates the successful incorporation of Cr^{3+} ions into the $BiFeO_3$ lattice without inducing structural distortions or phase transitions.[55,56] Unlike other transition metal, Cr substitution preserves the

fundamental crystallographic framework. This phase stability is crucial, as structural integrity directly impacts charge transport and recombination dynamics, both essential for consistent photocatalytic performance.

The morphological properties of BFCO nanoparticles are analyzed using TEM, as shown in Fig. 1(b) and (c). The high-resolution TEM (HRTEM) image in Fig. 1(b) reveals well-dispersed nanoparticles with distinct lattice fringes, indicating high crystallinity and phase purity. Additionally, selected area electron diffraction (SAED) analysis (Fig. 1(c)) displays scattered diffraction spots and incomplete concentric rings, confirming the material's polycrystalline nature. While the overall structure remains stable, slight deviations from ideal crystallography are observed, likely due to local lattice strain from Cr substitution. These distortions could influence the electronic band structure, potentially enhancing charge separation and extending carrier lifetimes, which are crucial for improving photocatalytic efficiency. Additionally, the polycrystalline structure promotes the formation of surface defects, such as oxygen vacancies, which act as active sites for ROS generation.

The FESEM image (Fig. 2(a)) reveals that the synthesized BFCO nanoparticles exhibit a well-dispersed nanoscale morphology, with an average particle size of 109 nm, as determined from the particle size distribution histogram (Fig. 2(b)). The small particle size enhances the specific surface area, facilitating greater pollutant adsorption and improved light absorption, which are crucial for efficient photocatalysis. Complementary elemental mapping images (Fig. 2(c)–(f)) confirm the uniform distribution of Bi, Fe, Cr, and O across the nanoparticle matrix, indicating the successful substitution of Fe by Cr without forming secondary phases. This homogeneous substitution plays a key role in modifying the electronic band structure, thereby enhancing visible-light absorption and boosting solar-light-driven photocatalytic activity. Furthermore, a comparison of the experimentally determined atomic and mass percentages with their theoretical values (Fig. S4 and Table S1†) validates the successful stoichiometric synthesis,
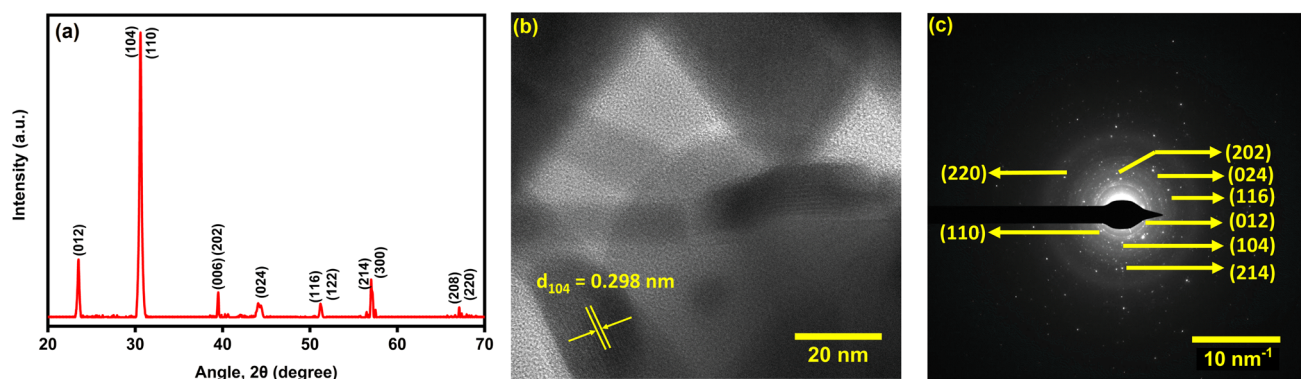

Fig. 1 Structural and morphological characterization of $BiFe_{0.5}Cr_{0.5}O_3$ nanoparticles (a) XRD pattern of $BiFe_{0.5}Cr_{0.5}O_3$ nanoparticles, confirming a single-phase perovskite structure with no secondary phases, indicating the successful substitution of Fe^{3+} with Cr^{3+} in the $BiFeO_3$ lattice. (b) HRTEM image displaying well-dispersed nanoparticles with clearly visible crystalline lattice fringes, verifying the high structural order and phase purity of $BiFe_{0.5}Cr_{0.5}O_3$ nanoparticles. (c) SAED pattern of $BiFe_{0.5}Cr_{0.5}O_3$ nanoparticles, exhibiting scattered diffraction spots and faint, incomplete concentric rings, indicative of a predominantly polycrystalline nature with slight deviations from the ideal crystallographic arrangement.
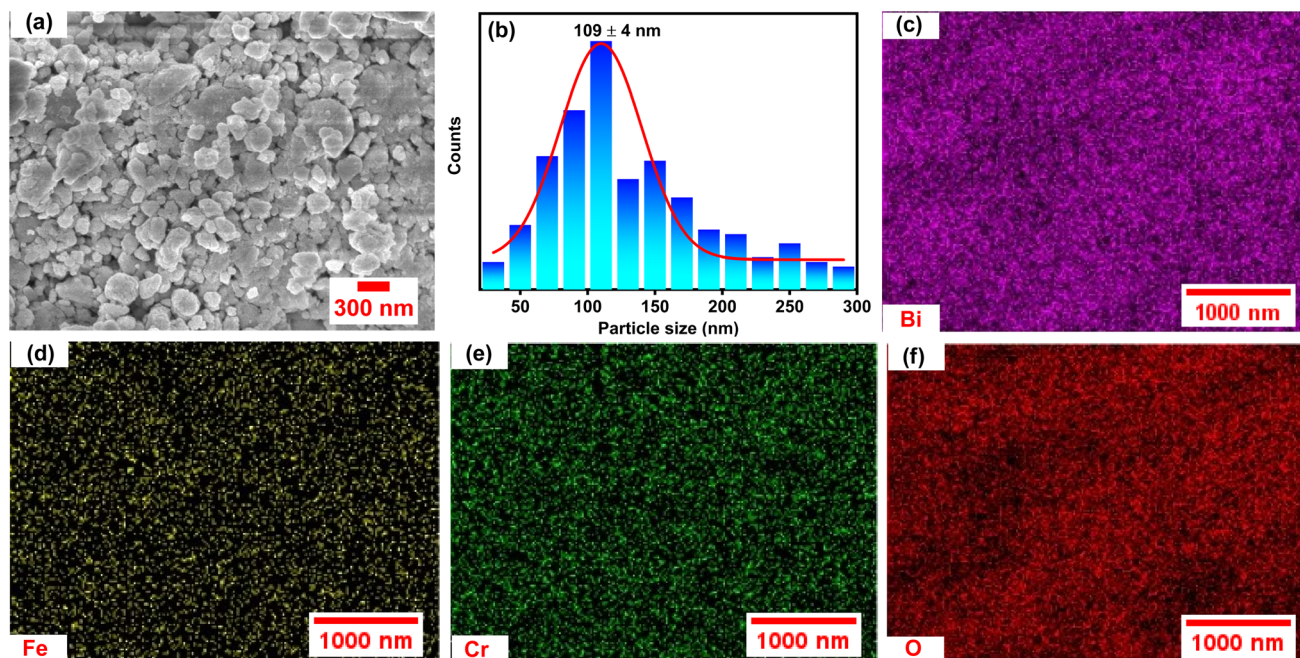
Fig. 2 Morphological and elemental analysis of BiFe$_{0.5}$Cr$_{0.5}$O$_3$ nanoparticles (a) FESEM image showing nanosized BiFe$_{0.5}$Cr$_{0.5}$O$_3$ particles, which contributes to a high surface area beneficial for photocatalysis. (b) Particle size distribution histogram indicating an average particle size of 109 nm. (c–f) Elemental mapping images confirming the homogeneous distribution of (c) Bi, (d) Fe, (e) Cr, and (f) O throughout the BiFe$_{0.5}$Cr$_{0.5}$O$_3$ nanoparticles, ensuring a well-integrated perovskite structure crucial for stable and efficient photocatalysis.

ensuring the structural and compositional stability of the nanoparticles.

To further understand the structural modifications induced by Cr substitution, Raman spectroscopy (Fig. 3(a)) provides insights into vibrational modes. Low-frequency peaks (140–180 cm^{-1}) correspond to Bi^{3+} vibrations, indicating structural distortions from the lone-pair effect, while Fe–O and Cr–O bending modes in the 220–400 cm^{-1} range validate the successful substitution of Fe^{3+} by Cr^{3+}, introducing octahedral distortions that influence charge transport dynamics.[59,60] The prominent peak near 560 cm^{-1}, assigned to A$_{1g}$ symmetric stretching of FeO$_6$/CrO$_6$ octahedra, further confirms lattice

stability.[59,60] More importantly, the broad band at 670–700 cm^{-1} is associated with oxygen vacancies, which play a crucial role in charge separation and suppress electron–hole recombination, enhancing photocatalytic efficiency.[61] Additional high-frequency spectral features (1000–1800 cm^{-1}) suggest defect-induced Raman scattering, indicative of non-stoichiometric oxygen states, while multi-phonon interactions in the 2500–3500 cm^{-1} region highlight strong electron–phonon coupling, facilitating charge transfer and extending carrier lifetimes for improved photocatalytic performance.

These structural modifications directly influence the temperature-dependent magnetic properties of BFCO
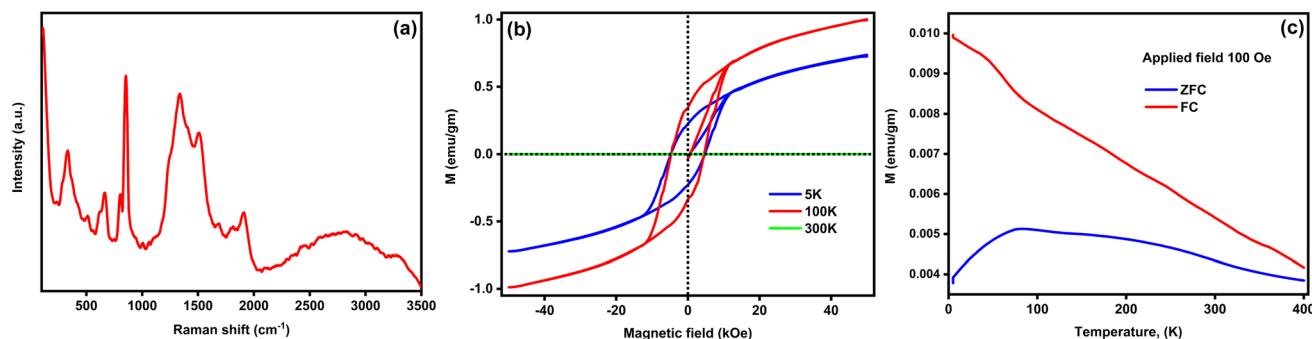

Fig. 3 Raman spectra and magnetic characteristics of BiFe$_{0.5}$Cr$_{0.5}$O$_3$ nanoparticles (a) Raman spectra of BiFe$_{0.5}$Cr$_{0.5}$O$_3$ nanoparticles, displaying characteristic vibrational modes associated with the perovskite structure. (b) M–H curves measured at different magnetic field strengths, demonstrating a weak ferromagnetic behavior in BiFe$_{0.5}$Cr$_{0.5}$O$_3$ due to spin canting effects and Cr substitution. The presence of remanence and coercivity confirms improved magnetic separation capabilities, facilitating easy recovery of the photocatalyst after reaction. (c) M–T curves were recorded under ZFC and FC conditions at an applied field of 100 Oe. The bifurcation between ZFC and FC curves suggests spin-glass-like behavior, indicating the influence of Cr substitution on magnetic interactions.

nanoparticles (Fig. 3(b)), which are critical for potential magnetic separation post-photocatalysis.[34] The magnetization (M) *vs.* the magnetic field (H) curves at 5 K and 100 K reveal finite coercivity (H_c) and remanent magnetization (M_r), confirming weak ferromagnetic (FM) or canted antiferromagnetic (AFM) interactions, while a slightly more open hysteresis loop at 100 K suggests competing FM–AFM interactions induced by Cr^{3+} substitution, leading to spin disorder and magnetic frustration.[55–57,62] At room temperature (300 K), the nearly linear magnetization curve with minimal hysteresis indicates a transition to a paramagnetic (PM) state due to thermal energy overcoming spin interactions. The field-cooled (FC) and zero-field-cooled (ZFC) magnetization curves (Fig. 3(c)) reveal a broad peak in the 100–150 K range, characteristic of a blocking temperature (T_b) associated with superparamagnetic (SPM) or spin-glass-like behavior.[55–57] This arises from finite-size effects, Cr^{3+}-induced spin canting, and competing FM–AFM interactions, leading to trapped magnetic moments below T_b. The persistence of weak FM interactions at ambient conditions,

despite spin-glass-like behavior at lower temperatures, supports the feasibility of BFCO nanoparticles as a dual-function material, offering both efficient photocatalytic degradation and magnetic recovery for catalyst reuse.

The optical and electronic properties of BFO and BFCO, illustrated in Fig. 4, highlight its strong potential as an efficient photocatalyst for pharmaceutical wastewater degradation. The optical band gap of BFCO nanoparticles was estimated using the UV absorption spectrum through Tauc's relation:

$$(\alpha h\nu)^{1/\gamma} = B(h\nu - E_g)$$

where h represents Planck's constant, ν is the photon frequency, E_g is the band gap energy, and B is a material-dependent constant. For direct electronic transitions, the value of γ is taken as 1/2. The band gap energy of BFCO nanoparticles was obtained from the x-intercept of the plot of $(\alpha h\nu)^{1/\gamma}$ *versus* E_g. The Tauc plot[52,63] (Fig. 4(a)) reveals a direct bandgap of 1.87 eV, which is significantly lower than that of pristine BFO nanoparticles
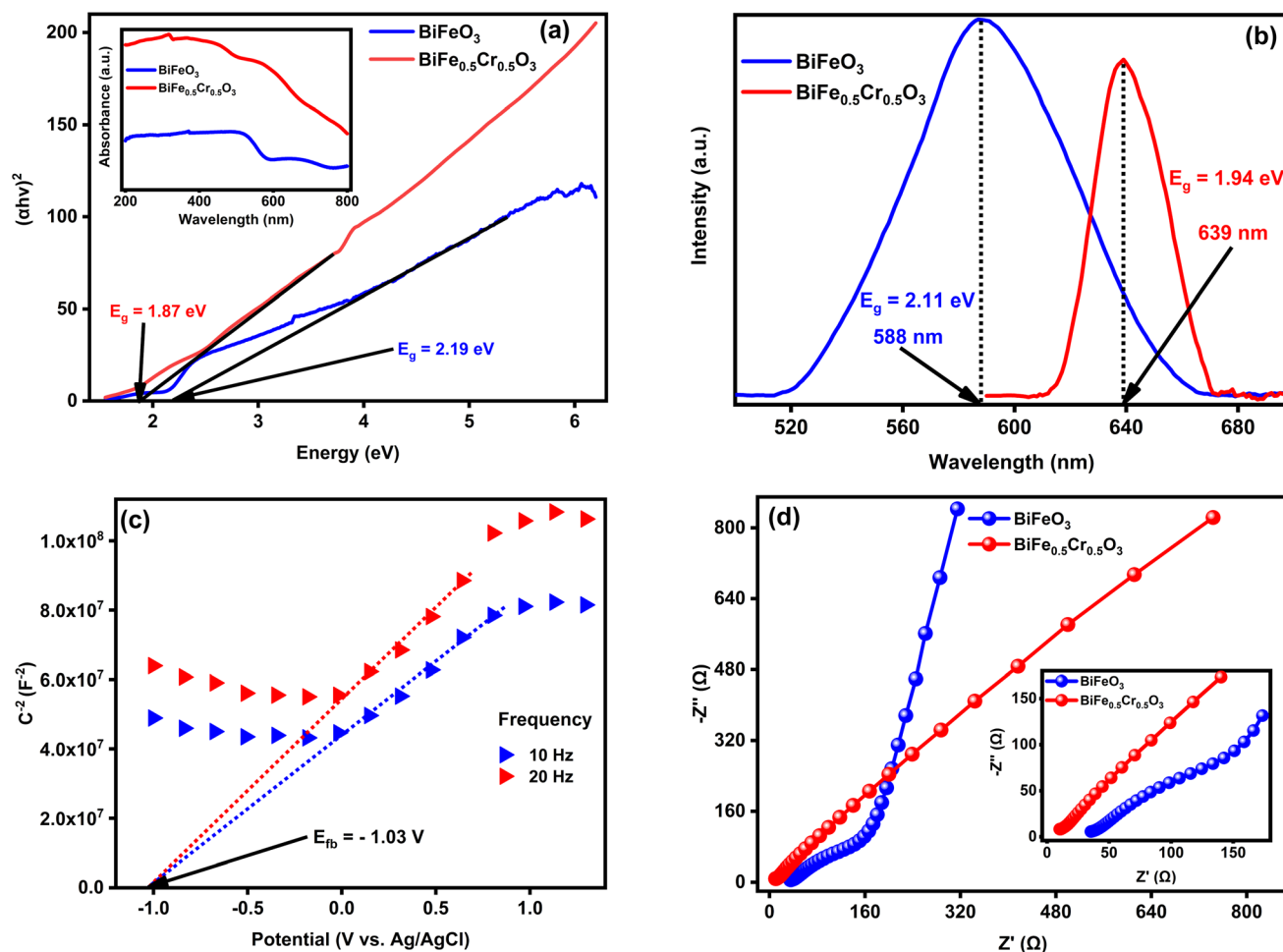

Fig. 4 Optoelectronic and charge transfer properties of $BiFeO_3$ and $BiFe_{0.5}Cr_{0.5}O_3$ nanoparticles. (a) Tauc plots indicating a reduction in the direct bandgap of $BiFe_{0.5}Cr_{0.5}O_3$ compared to pristine $BiFeO_3$, suggesting improved absorption in the visible light region. The inset shows the corresponding UV–vis absorption spectra of both samples. (b) Steady-state photoluminescence (PL) spectra, displaying lower emission intensity and a red-shifted peak for $BiFe_{0.5}Cr_{0.5}O_3$, in agreement with the bandgap narrowing observed in the Tauc analysis. (c) Mott–Schottky plots recorded at different frequencies, confirming the n-type semiconducting nature of $BiFe_{0.5}Cr_{0.5}O_3$. (d) Nyquist plots illustrating reduced charge transfer resistance (R_{ct}) for $BiFe_{0.5}Cr_{0.5}O_3$ in comparison to $BiFeO_3$, with the inset emphasizing the high-frequency region for better visualization.

(2.19 eV).[34] This reduction in bandgap enhances BFCO's ability to absorb visible light more effectively, thereby improving its solar energy utilization for photocatalytic applications. The UV-vis absorption spectrum (inset) further supports this broad absorption capability, while the steady-state PL spectrum (Fig. 4(b)) confirms the optical band structure determination with an emission peak corresponding to the bandgap. A relatively low PL intensity of BFCO compared BFO nanoparticles indicates suppressed electron–hole recombination, which extends charge carrier lifetimes and enhances photocatalytic efficiency. Further electronic insights are provided by Mott–Schottky analysis[52,64–66] (Fig. 4(c)), which confirms BFCO's n-type semiconductor nature with a flat band potential of −1.03 V vs. Ag/AgCl. Combining this with the bandgap data, the conduction band minimum (CBM) and valence band maximum (VBM) were calculated as −0.93 V and 0.95 V vs. NHE, respectively, facilitating redox reactions essential for pollutant degradation. Charge transport dynamics were also investigated through EIS analysis.[54,67] The Nyquist plots in Fig. 4(d) reveal a reduced charge transfer resistance (R_{ct}) and improved charge separation of BFCO compared to BFO nanoparticles, which contribute to BFCO's superior photocatalytic performance.

To evaluate the photoresponse characteristics of the synthesized BFCO nanoparticles, photoelectrochemical measurements including CV, LSV, and EIS were conducted under both dark and illuminated conditions,[28] as presented in Fig. 5. The CV curves (Fig. 5(a)) of the symmetric $BiFe_{0.5}Cr_{0.5}O_3 \| BiFe_{0.5}Cr_{0.5}O_3$ cell exhibit significantly enhanced current densities under light irradiation, indicating improved photoresponse behavior due to more efficient charge separation and increased carrier mobility upon illumination. This enhancement reflects the effective utilization of solar energy to facilitate redox reactions at the electrode–electrolyte interface. Similarly, the LSV results (Fig. 5(b)) further support this observation, showing consistently higher photocurrent densities under illumination across the potential window. This indicates enhanced generation and transport of photoinduced charge carriers, demonstrating the material's strong photoactivity. Additionally, EIS analysis (Fig. 5(c)) reveals a notable decrease in the semicircle diameter of the Nyquist plots under light, signifying

reduced charge transfer resistance (R_{ct}) and improved interfacial charge transport. The inset highlights this trend more clearly in the high-frequency region, while the shift of the impedance arc toward lower Z' values under illumination further confirms enhanced charge dynamics.

To understand the chemical states and surface composition of BFCO, XPS was conducted, as illustrated in Fig. 6. The survey spectrum (Fig. 6(a)) confirms the presence of Bi, Fe, Cr, and O, verifying the chemical purity and stoichiometric integrity of the synthesized nanoparticles. High-resolution spectra of individual elements provide deeper insights into their oxidation states and electronic interactions (details in ESI Table S2†). The Bi 4f spectrum (Fig. 6(b)) shows characteristic peaks corresponding to Bi^{3+}, confirming its expected valency in the perovskite structure.[34] Similarly, the Fe 2p spectrum (Fig. 6(c)) indicates a mixed-valence state of Fe^{3+}/Fe^{2+}, which enhances internal charge transfer and reduces recombination losses.[52] The Cr 2p spectrum (Fig. 6(d)) also exhibits Cr^{3+} as the dominant oxidation state, with minor contributions from Cr^{2+}, facilitating efficient electron transfer.[53] The O 1s spectrum (Fig. 6(e)) reveals three primary components: lattice oxygen (O^{2-}), oxygen vacancies, and surface hydroxyl groups.[52,68,69] Notably, the presence of oxygen vacancies (530.6 eV) suggests significant defect concentration, which enhances photocatalysis by promoting pollutant adsorption and ROS generation.[52] Additionally, surface hydroxyl groups (532.45 eV) contribute to the formation of hydroxyl radicals (˙OH), further improving the degradation efficiency of pharmaceutical contaminants.[52]

The valence band (VB) XPS analysis (Fig. 6(f)) confirms a VBM of 0.95 eV, aligning well with the Mott–Schottky analysis and reinforcing the favorable band alignment of BFCO for photocatalytic applications. The combination of its suitable band structure, efficient charge transport, and favorable surface chemistry establishes BFCO as a highly promising material for visible-light-driven wastewater remediation.

3.2 Photocatalytic performances evaluation

In photocatalytic antibiotic wastewater treatment, the optimization of catalyst dosage, pollutant concentration, and solution
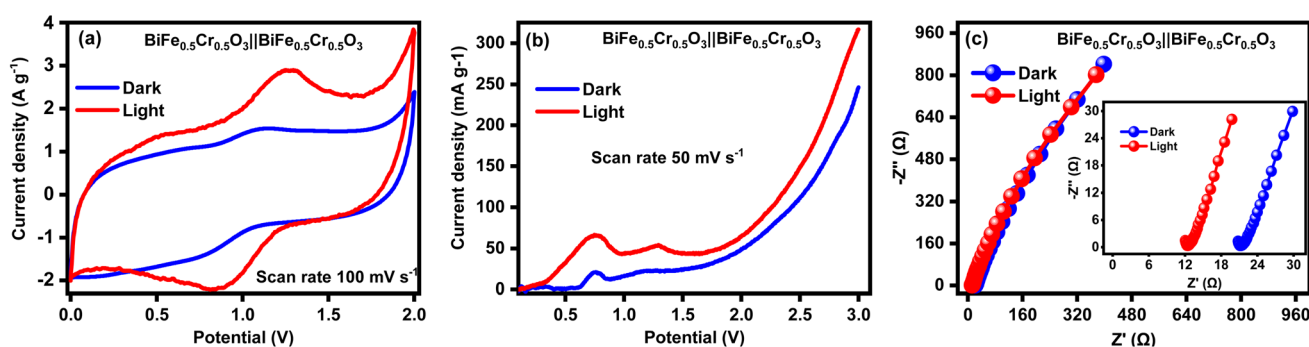

Fig. 5 Photoelectrochemical performance of $BiFe_{0.5}Cr_{0.5}O_3 \| BiFe_{0.5}Cr_{0.5}O_3$ under dark and light conditions. (a) CV curves showing enhanced current density under light due to improved charge separation; (b) LSV curves confirming higher photocurrent generation under illumination; (c) Nyquist plots revealing reduced charge transfer resistance under light, with the inset highlights the high-frequency region, clearly showing improved interfacial charge transfer dynamics upon light activation.
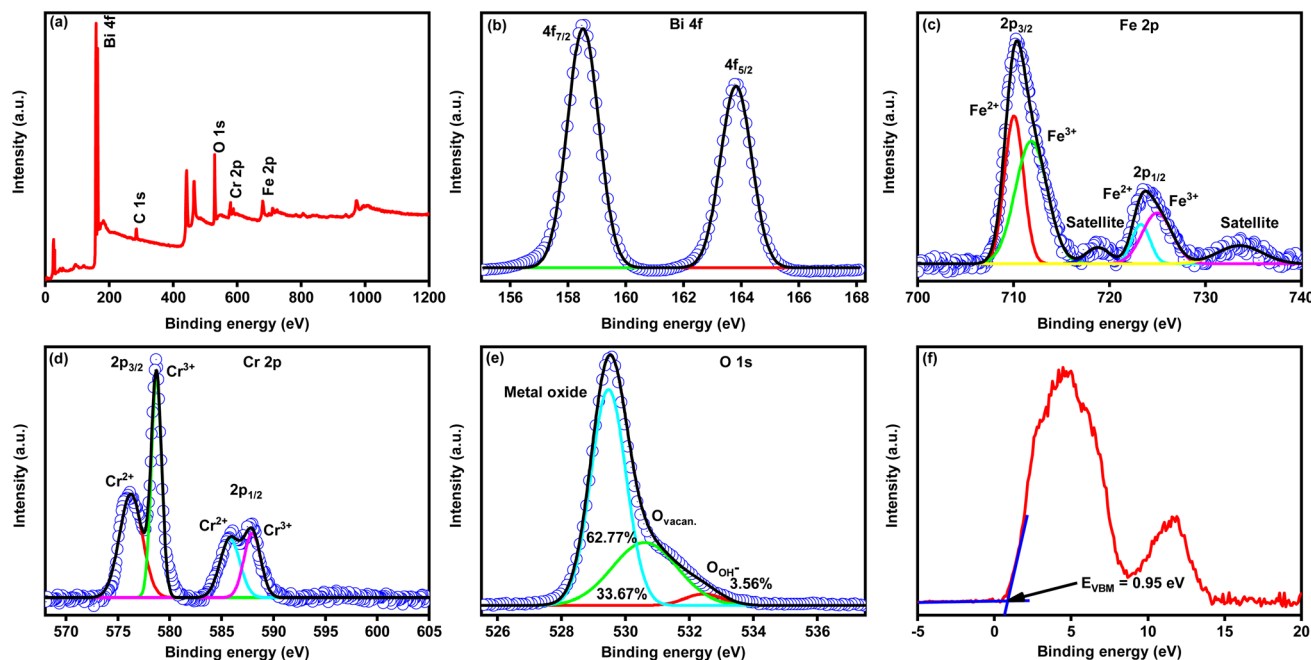
Fig. 6 Surface chemical states and electronic structure of BiFe$_{0.5}$Cr$_{0.5}$O$_3$ nanoparticles *via* XPS (a) XPS survey spectrum displaying distinct peaks for Bi 4f, Fe 2p, Cr 2p, and O 1s core levels, confirming the presence of Bi^{4+}, Fe^{2+}/Fe^{3+}, Cr^{2+}/Cr^{3+}, and O^{2-} species. High-resolution XPS spectra of (b) Bi 4f, (c) Fe 2p, (d) Cr 2p, and (e) O 1s, indicating the detailed binding energies and confirming the chemical states of each element. Specifically, the high-resolution O 1s spectrum shows distinct peaks at 530.6 eV (oxygen vacancies) and 532.45 eV (surface hydroxyl groups), indicating the presence of oxygen vacancies and OH groups. These defects enhance photocatalytic performance by trapping charge carriers and facilitating reactive oxygen species (ROS) generation. (f) Valence band XPS spectrum showing a valence band maximum (VBM) of 0.95 eV, closely matching the Mott–Schottky analysis results and further validating the electronic structure of BiFe$_{0.5}$Cr$_{0.5}$O$_3$ nanoparticles.

pH plays a critical role in achieving maximum degradation efficiency. Accordingly, these parameters were systematically varied, and the corresponding results are presented in Fig. 7.

To begin with, the effect of catalyst dosage on photocatalytic performance was investigated by employing 10 mg, 20 mg, and 30 mg of BFCO (Fig. 7(a) and (d)). The degradation efficiencies of both CIP and LFX increased with higher catalyst dosages. This enhancement can be attributed to the increased number of active surface sites and greater generation of reactive oxygen species under visible light irradiation. However, the difference in photocatalytic activity between 20 mg and 30 mg was minimal, suggesting a saturation effect at elevated catalyst concentrations. At higher dosages, particle agglomeration and excessive light scattering may occur, thereby limiting the effective utilization of the photocatalyst. Based on these observations, 20 mg was identified as the optimal catalyst dosage and was subsequently used in all further photocatalytic experiments.

Next, the influence of pollutant concentration on degradation kinetics was evaluated by varying the initial concentrations of CIP and LFX (1.4 mg, 2 mg, and 2.6 mg) (Fig. 7(b) and (e)). The results revealed that lower pollutant concentrations favored higher degradation efficiencies. This behavior is attributed to the finite number of active sites on the photocatalyst surface, which may become saturated at higher pollutant loads. Furthermore, elevated pollutant concentrations can increase solution turbidity, thereby reducing light penetration and limiting the generation of reactive species essential for photocatalysis.

Finally, the effect of solution pH on photocatalytic activity was studied under acidic (pH 2.7), neutral (pH 7), and basic (pH 11) conditions (Fig. 7(c) and (f)). The results indicated that the degradation efficiencies of both antibiotics were significantly higher in acidic and basic media compared to neutral pH. This enhanced performance under extreme pH conditions is likely due to changes in the surface charge of the photocatalyst and the ionization state of the antibiotic molecules. Such changes promote stronger electrostatic interactions and facilitate the formation of highly reactive oxygen species.

The time-dependent UV-vis absorption spectra (Fig. 8(a) and (b)) illustrate a continuous reduction in peak intensity for CIP and LFX, accompanied by a noticeable hypsochromic shift.[64,70] This shift signifies molecular degradation rather than mere surface adsorption, indicating the breakdown of complex antibiotic structures into smaller, less harmful byproducts. The steady decline in absorbance intensity confirms BFCO's efficient photocatalytic activity in accelerating pollutant decomposition. The degradation efficiency, depicted in Fig. 8(c), was calculated using the equation:[34,51,52,71]

$$\text{Photocatalytic degradation (\%)} = \left(\frac{C_0 - C}{C_0}\right) \times 100$$

where C_0 is the initial pollutant concentration, and C represents the concentration at a given irradiation time. BFCO nanoparticles achieved 70.35% degradation efficiency for CIP and a significantly higher 94% for LFX, outperforming pristine BiFeO$_3$, which degraded only 42% and 46% of CIP and LFX[34]
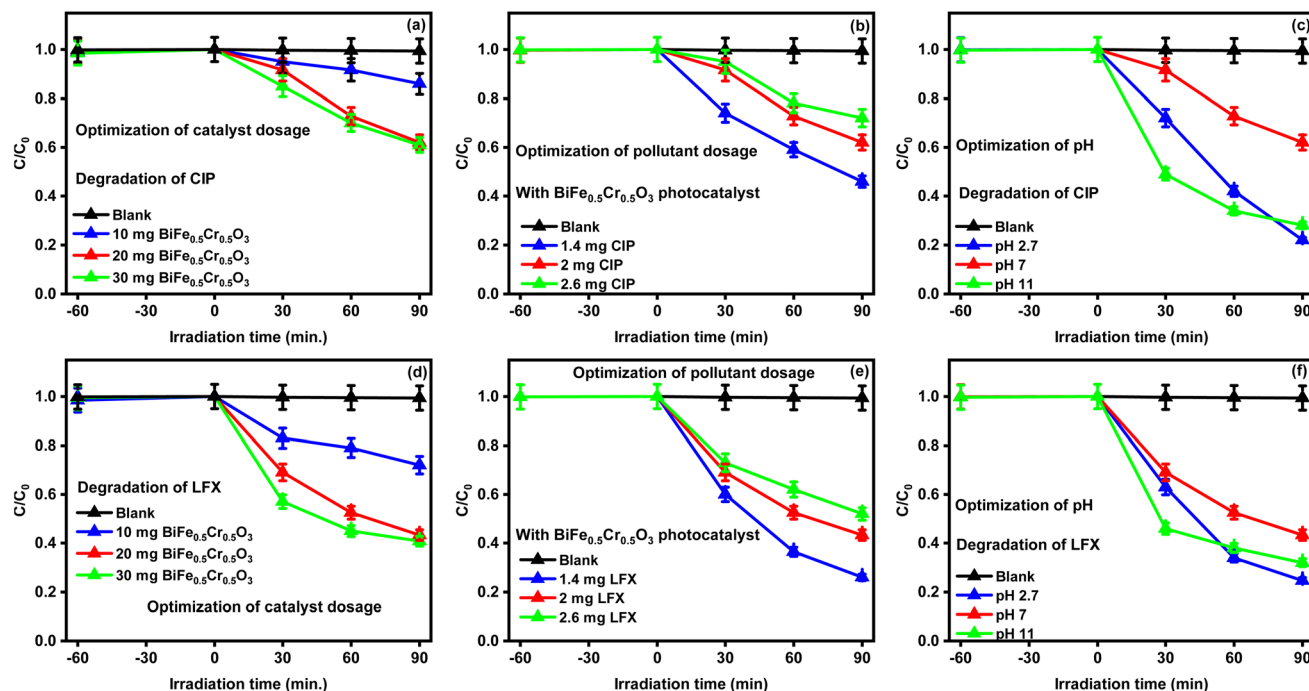
Fig. 7 Optimization of photocatalytic degradation parameters for CIP and LFX using BiFe$_{0.5}$Cr$_{0.5}$O$_3$ photocatalyst under solar irradiation. (a and d) Effect of catalyst dosage (10 mg, 20 mg, and 30 mg) on the degradation of CIP and LFX, respectively. The degradation efficiency improved with increasing catalyst dosage and a saturation trend was observed beyond 20 mg. (b and e) Effect of pollutant concentration (1.4 mg, 2 mg, and 2.6 mg) on the degradation of CIP and LFX. Higher initial concentrations reduced degradation efficiency due to active site saturation and limited light penetration. (c and f) Effect of solution pH (2.7, 7, and 11) on the photocatalytic activity for CIP and LFX. Enhanced degradation was observed at acidic and basic pH values due to favorable surface charge interactions and increased formation of reactive oxygen species.

(shown in ESI Fig. S5†), respectively, under identical condition. This enhanced performance is attributed to oxygen vacancies and optimized band edge positions, which facilitate efficient charge carrier separation and ROS generation. Oxygen vacancies serve as active sites for pollutant adsorption and photocatalytic reactions, while well-aligned conduction and valence bands enable effective oxidation and reduction processes. The superior degradation efficiency of LFX suggests stronger interactions with ROS due to differences in molecular structure and adsorption affinity on the BFCO surface. Notably, to validate the role of light in the photocatalytic degradation process and to distinguish true photocatalytic activity from simple photolysis or adsorption effects, control experiments were conducted in the absence of the BFCO photocatalyst, as presented in ESI Fig. S6.† In these experiments, ciprofloxacin and levofloxacin were exposed to solar irradiation under identical condition. The results showed negligible degradation of both pollutants without the catalyst, confirming that light alone does not significantly contribute to their degradation. These findings highlight the essential role of the BFCO photocatalyst in facilitating the photocatalytic degradation process.

To analyze reaction kinetics, a pseudo-first-order kinetic model was applied:[34,51,52,71]

$$\ln\left(\frac{C_0}{C}\right) = kt$$

where k is the reaction rate constant and t is the irradiation time. The linear correlation in the $\ln(C_0/C)$ *vs.* time plot

(Fig. 8(d)) confirms first-order kinetics, indicating that the reaction rate depends directly on pollutant concentration. The high rate constants for CIP and LFX reflect BFCO's rapid degradation capability, enabled by efficient charge carrier dynamics and minimized recombination losses. The comparative analysis presented in Table 1 highlights the superior photocatalytic degradation performance of our synthesized BiFe$_{0.5}$Cr$_{0.5}$O$_3$ nanoparticles for pharmaceutical wastewater treatment. Notably, our BiFe$_{0.5}$Cr$_{0.5}$O$_3$ catalyst achieved 70.35% degradation of CIP and 94% degradation of LFX under 500 W Hg–Xe light within 240 minutes, outperforming or matching the efficiencies of other BFO-based photocatalysts reported in recent studies. For instance, La-doped BFO and Gd-doped BFO demonstrated degradation efficiencies ranging from 71% to 34.2% under varying conditions,[34,74] while co-doped systems such as Gd–Sn and Sm–Mn exhibited comparable or lower efficiencies.[44,47] These findings establish BFCO as an effective and promising photocatalyst for pharmaceutical pollutant degradation, demonstrating enhanced efficiency in breaking down antibiotics under solar-mimicking conditions.

3.3 Activation energy calculation

The efficiency of a photocatalyst is influenced by its ability to lower the activation energy (E_a) for pollutant degradation. As shown in Fig. 9(a) and (b), the degradation of LFX under varying temperature conditions demonstrates its thermally activated nature, with increasing reaction rate constants at higher
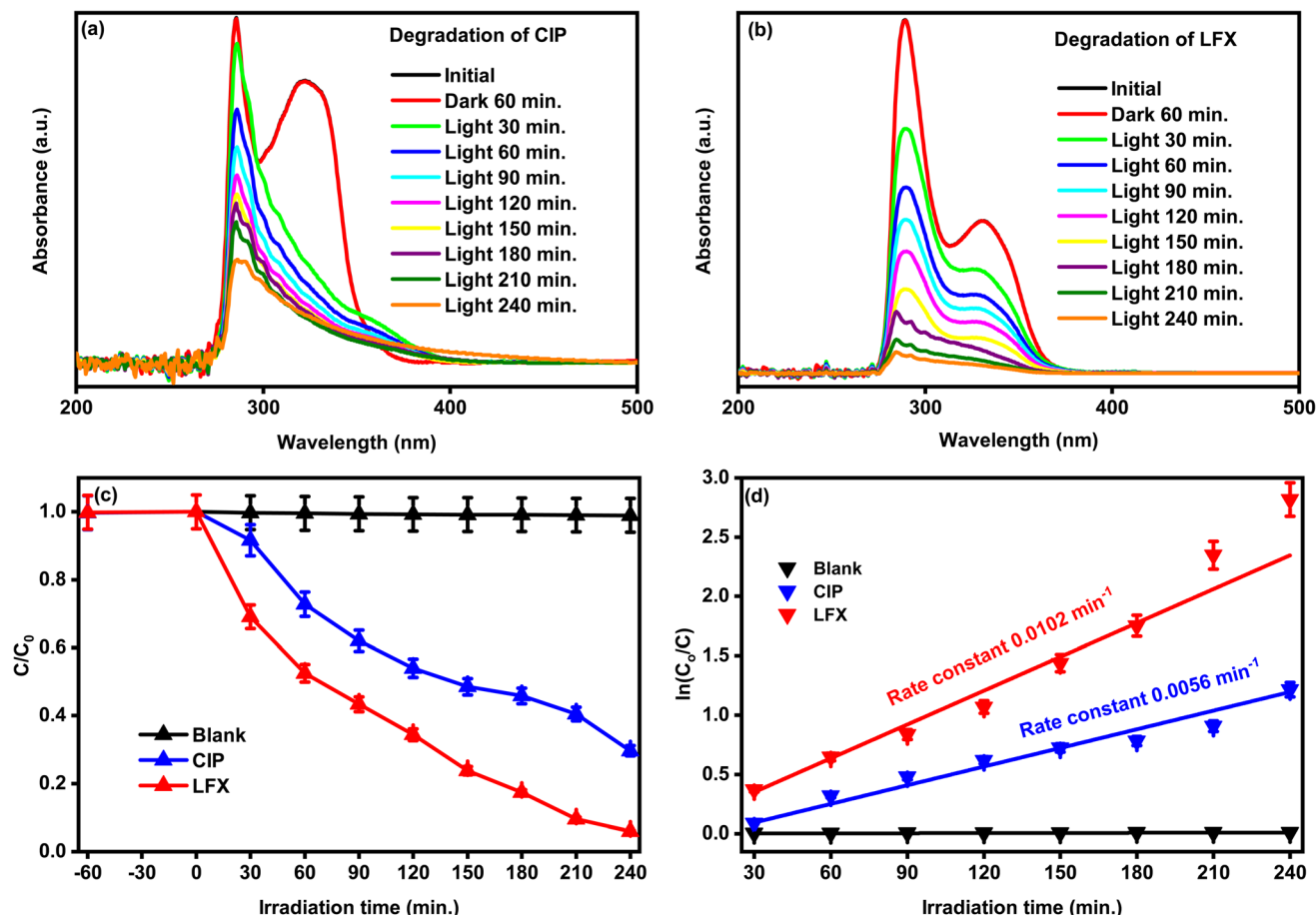
Fig. 8 Photocatalytic degradation of CIP and LFX by $BiFe_{0.5}Cr_{0.5}O_3$ nanoparticles under solar light irradiation. UV-Vis absorption spectra showing the progressive degradation of (a) CIP and (b) LFX over time under solar light irradiation. The gradual decrease in absorbance intensity confirms the efficient photocatalytic breakdown of these pharmaceutical pollutants. (c) Photocatalytic degradation efficiency after 240 minutes of irradiation using a 500 W Hg–Xe lamp, where $BiFe_{0.5}Cr_{0.5}O_3$ nanoparticles achieved 70.35% degradation of CIP and 94% degradation of LFX, highlighting their superior photocatalytic activity. (d) Pseudo-first-order kinetic analysis illustrating the enhanced degradation rate for both CIP and LFX in the presence of $BiFe_{0.5}Cr_{0.5}O_3$. The kinetic rate constants indicate faster decomposition in comparison to control experiments, demonstrating the effectiveness of $BiFe_{0.5}Cr_{0.5}O_3$ as a high-performance photocatalyst for pharmaceutical wastewater treatment.

Table 1 A brief review of the pollutant degrading capabilities exhibited by $BiFe_{0.5}Cr_{0.5}O_3$ nanoparticles photocatalyst compared to other commonly used photocatalysts in recent investigations. This table suggests that our synthesized $BiFe_{0.5}Cr_{0.5}O_3$ nanoparticles photocatalyst exhibited superior photocatalytic degradation performances on pharmaceutical antibiotics surpassing or comparable with the other photocatalysts

| Perovskite	Light source	Synthesis method	Pollutant	Irradiation time (min)	Degradation (%)	Ref.
15% La-doped $BiFeO_3$	—	Co-precipitation	Doxorubicin	300	93	72
20% La-doped $BiFeO_3$	300 W Xe	Sol–gel	Methylene blue	300	71	73
10% La-doped $BiFeO_3$	500 W Hg–Xe	Sol–gel	Ciprofloxacin	240	70	34
			Levofloxacin	240	71	
1% Gd-doped $BiFeO_3$	300 W Xe	Sol–gel	Rhodamine B	270	34.2	74
3% Gd-doped $BiFeO_3$	300 W Xe	Sol–gel	Rhodamine B	270	56.8	74
5% Gd-doped $BiFeO_3$	300 W Xe	Sol–gel	Ciprofloxacin	270	42.1	74
Gd and Sn co-doped $BiFeO_3$	300 W Xe	Sol–gel	Methylene blue	180	68	44
			Congo red	180	72	
Sm and Mn co-doped $BiFeO_3$	—	Double solvent Sol–gel	Methylene blue	180	52	47
			Methyl violet	180	60	
$BiFe_{0.5}Cr_{0.5}O_3$	500 W Hg–Xe	Sol–gel	Ciprofloxacin	240	70.35	This work
			Levofloxacin	240	94	
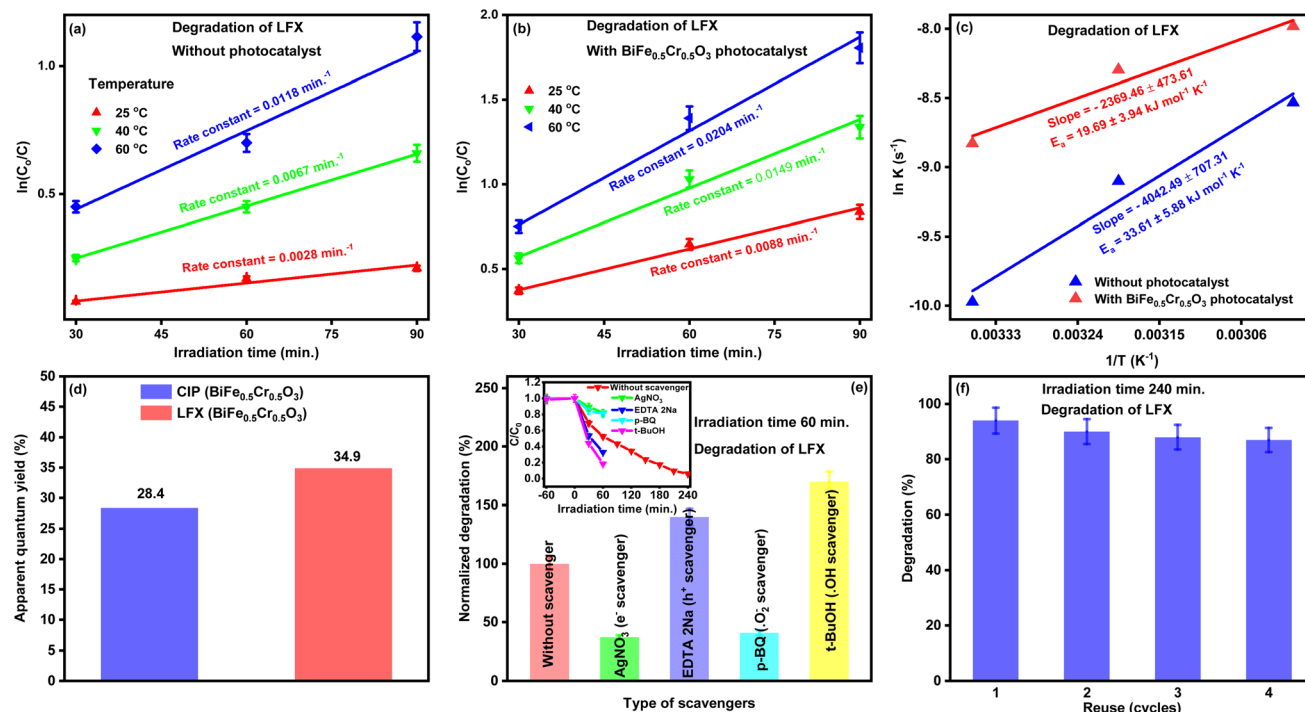
Fig. 9 Kinetics, activation energy, quantum efficiency, and reusability of BiFe$_{0.5}$Cr$_{0.5}$O$_3$ nanoparticles for photocatalytic degradation of pharmaceutical pollutants ln(C_0/C) *vs.* irradiation time plots for the degradation of LFX at 25 °C, 40 °C, and 60 °C, comparing reaction kinetics (a) without and (b) with the presence of BiFe$_{0.5}$Cr$_{0.5}$O$_3$ nanoparticles as a photocatalyst. The degradation rate is significantly enhanced in the presence of BiFe$_{0.5}$Cr$_{0.5}$O$_3$, demonstrating the catalyst's role in facilitating pollutant breakdown under solar irradiation. (c) Arrhenius plot (ln(k) *vs.* 1/T) for LFX degradation, comparing the activation energy (E_a) with and without the presence of BiFe$_{0.5}$Cr$_{0.5}$O$_3$ photocatalyst. The reduced activation energy in the presence of BiFe$_{0.5}$Cr$_{0.5}$O$_3$ indicates a more efficient degradation process, suggesting improved charge transfer dynamics and stronger interactions between the photocatalyst and pollutant molecules. (d) AQY measurements for the degradation of CIP and LFX, demonstrating high energy efficiency of BiFe$_{0.5}$Cr$_{0.5}$O$_3$ nanoparticles under solar light irradiation. (e) Scavenger experiments using AgNO$_3$ (electron scavenger), EDTA–2Na (hole scavenger), benzoquinone (*p*-BQ) (superoxide radical scavenger), and *tert*-butyl alcohol (*t*-BuOH) (hydroxyl radical scavenger) reveal that electrons and superoxide radicals play the dominant role in pollutant degradation. (f) Reusability study showing consistent photocatalytic activity of BiFe$_{0.5}$Cr$_{0.5}$O$_3$ over multiple degradation cycles, confirming its excellent stability and durability.

temperatures. Activation energy was determined using the Arrhenius equation:[52,75,76]

$$\ln(k) = \ln(A) - \frac{E_a}{RT}$$

where A is the pre-exponential factor, R is the universal gas constant, and T is temperature in Kelvin. The activation energy in the absence of BFCO was 33.61 ± 5.88 kJ mol^{-1} K^{-1}, whereas with BFCO, it was significantly reduced to 19.69 ± 3.94 kJ mol^{-1} K^{-1} (Fig. 9(c)). This reduction highlights BFCO's ability to lower the energy barrier for degradation, thereby enhancing reaction kinetics under solar irradiation. The Cr^{3+} substitution and oxygen vacancies improve charge carrier separation, reducing recombination and facilitating redox reactions.

3.4 Apparent quantum yield (AQY) calculation

The AQY analysis (Fig. 9(d)) further validates BFCO's efficiency in solar-driven photocatalysis, we calculated the AQY by the following equation:[52,77–79]

$$AQY \ (\%) = \frac{\text{number of degraded molecules}}{\text{number of incident photons}} \times 100.$$

The AQY values were 28.4% for CIP and 34.9% for LFX, reflecting effective photon utilization in degradation reactions. BFCO's high AQY stems from its narrow bandgap, which enhances visible-light absorption, and optimized band structure, which ensures efficient charge transfer. The ability to maintain high AQY under natural light underscores BFCO's potential as an environmentally sustainable photocatalyst for large-scale wastewater treatment.

3.5 Active species trapping experiments

A mechanistic study using selective scavenger experiments (Fig. 9(e)) identified the dominant reactive species in the degradation process.[51,80] The incorporation of AgNO$_3$, an electron scavenger, led to a marked decrease in degradation efficiency, implicating photogenerated electrons in the formation of superoxide radicals (O$_2^{-\bullet}$). Likewise, the incorporation of *p*-benzoquinone, a specific superoxide radical scavenger, similarly diminished LFX removal, further confirming the critical role of O$_2^{-\bullet}$ in the reaction pathway. In contrast, the presence of EDTA–2Na (a hole scavenger) and *tert*-butyl alcohol (a hydroxyl radical scavenger) resulted in enhanced degradation rates, indicating that neither photogenerated holes nor hydroxyl

radicals contribute significantly to LFX degradation. This observation is consistent with the valence band maximum of BFCO, which lies at a potential insufficient for hydroxyl radical generation *via* hole oxidation. Collectively, these results demonstrate that photogenerated electrons and subsequent superoxide radical formation constitute the dominant oxidative pathway for LFX degradation in the BFCO system, in agreement with the nanoparticle band-edge positions analysis.

3.6 Reusability and post-cycle characterizations

The stability of BFCO nanoparticles was assessed over four consecutive photocatalytic cycles (Fig. 9(f)), revealing consistently high degradation efficiency. The observed decrease in photocatalytic activity upon recycling may be attributed to a slight reduction in crystallinity and a marginal increase in particle agglomeration during the reuse process. These changes can diminish the number of accessible active sites and impede efficient charge carrier generation and transfer. Furthermore, repeated exposure to reactive oxygen species and intermediate degradation products may lead to partial surface fouling or the blockage of active sites. Nonetheless, the overall decline in photocatalytic performance remains minimal and within an acceptable range, indicating the structural and functional stability of the BFCO nanocatalyst under repeated use. The structural integrity of BFCO after repeated cycles was analyzed

using XRD, FESEM, and UV-Vis optical characterization. XRD spectra (Fig. 10(a) and (b)) show a slight reduction in crystallinity due to prolonged photocatalytic reactions, but the absence of peak shifts or impurity phases confirms phase stability. FESEM images before (Fig. 10(c)) and after (Fig. 10(d)) four cycles indicate that BFCO retains its nanoscale morphology without significant aggregation or degradation. Tauc plots (Fig. 10(e) and (f)) confirm that the bandgap remains stable across multiple cycles, ensuring consistent photocatalytic performance. Overall, BFCO nanoparticles exhibit excellent structural, morphological, and optical stability, reinforcing their potential as a reusable and efficient photocatalyst for pharmaceutical wastewater treatment.

3.7 Photocatalysis mechanism

The photocatalytic degradation of pharmaceutical pollutants such as CIP and LFX using BFCO nanoparticles involves multiple interdependent steps, including light absorption, charge carrier generation, redox reactions, ROS formation, and stepwise mineralization of contaminants into non-toxic end products.[34,52,64] Fig. 11 presents a schematic representation of this mechanism, highlighting how BFCO effectively degrades pharmaceutical contaminants under solar light irradiation. The efficiency of this process is significantly enhanced by oxygen vacancies, mixed-valence states, and optimized band edge positions in BFCO,
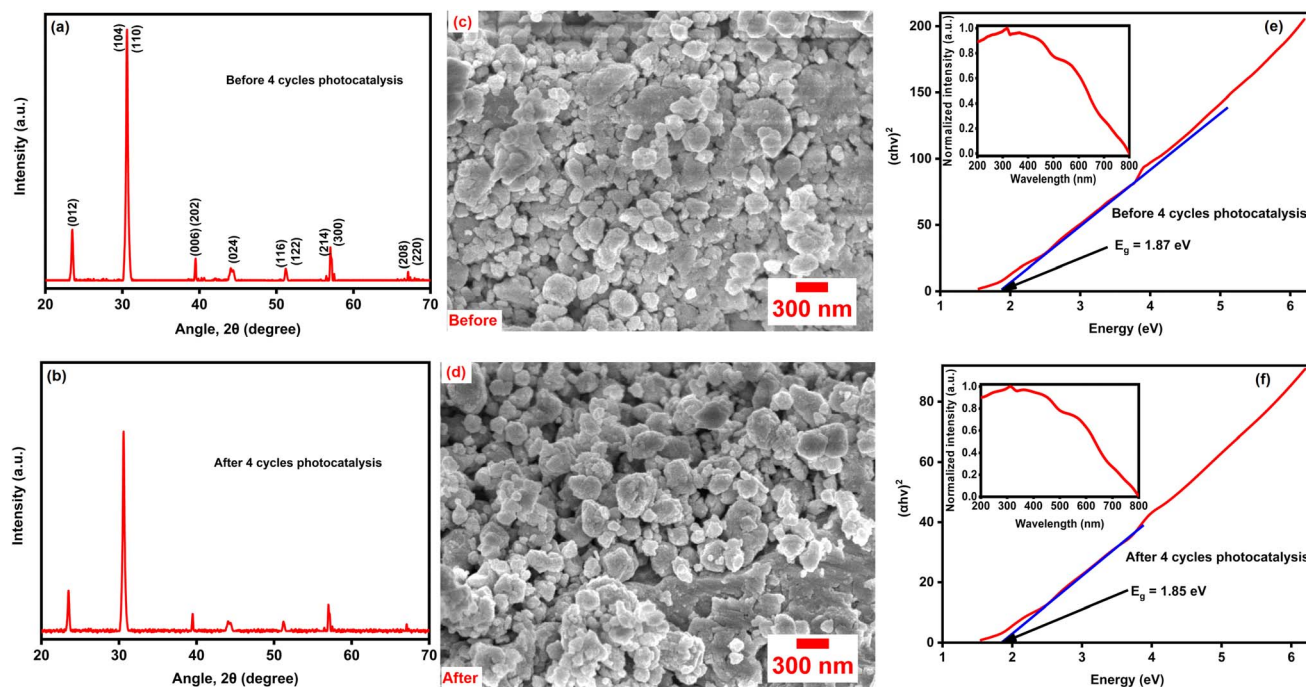

Fig. 10 Structural, morphological, and optical stability of $BiFe_{0.5}Cr_{0.5}O_3$ nanoparticles after multiple photocatalytic cycles. XRD spectra of $BiFe_{0.5}Cr_{0.5}O_3$ nanoparticles (a) before and (b) after four photocatalytic cycles, showing a slight reduction in crystallinity due to prolonged photocatalytic activity. However, the consistent peak positions and shapes confirm the overall structural integrity of the material, which is essential for maintaining high photocatalytic efficiency over repeated use. FESEM images of $BiFe_{0.5}Cr_{0.5}O_3$ nanoparticles (c) before and (d) after four photocatalytic cycles, demonstrating morphological stability with no significant structural degradation. The well-preserved nanostructure ensures sustained surface activity for photocatalytic reactions. Tauc plots of $BiFe_{0.5}Cr_{0.5}O_3$ (e) before and (f) after four photocatalytic cycles, revealing a consistent bandgap value, confirming that the fundamental electronic properties of the material remain unchanged. The insets show UV-Vis absorbance spectra, demonstrating no significant loss in light absorption ability, reinforcing the long-term stability and reusability of $BiFe_{0.5}Cr_{0.5}O_3$ for wastewater treatment applications.
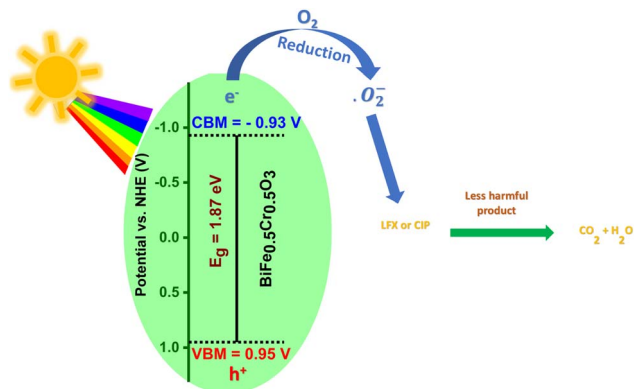
**Fig. 11** Photocatalytic degradation mechanism of CIP or LFX using $BiFe_{0.5}Cr_{0.5}O_3$ nanoparticles as a photocatalyst. Upon solar light absorption, $BiFe_{0.5}Cr_{0.5}O_3$ generates electron–hole pairs (e^-/h^+), initiating redox reactions with water and oxygen to produce superoxide ($O_2^{\bullet-}$) radicals. These reactive species effectively degrade CIP and LFX into harmless byproducts (CO_2 and H_2O).

which collectively improve charge carrier dynamics, suppress recombination, and promote efficient redox reactions.

3.7.1 Photoexcitation and charge carrier generation. Upon exposure to solar light, BFCO absorbs photons with energy equal to or greater than its bandgap (1.87 eV). This results in the excitation of electrons from the valence band (VB) to the conduction band (CB), leaving behind positively charged holes (h^+) in the VB:

$$BFCO + h\nu \rightarrow e_{CB}^- + h_{VB}^+$$
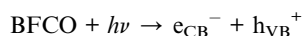
The photogenerated charge carriers play a crucial role in initiating redox reactions necessary for pollutant degradation. The presence of oxygen vacancies in BFCO suppresses electron–hole recombination by trapping charge carriers, ensuring that a higher fraction of electrons and holes participate in photocatalytic processes.

3.7.2 Generation of ROS. The electrons in the conduction band and the holes in the valence band drive the formation of ROS, which play a vital role in breaking down CIP and LFX.

Reduction reactions: superoxide radical formation ($O_2^{\bullet-}$):

The photogenerated electrons in the CB migrate to the surface of BFCO, where they interact with dissolved molecular oxygen (O_2), reducing it to highly reactive superoxide radicals ($O_2^{\bullet-}$):

$$O_2 + e_{CB}^- \rightarrow O_2^{\bullet-}$$
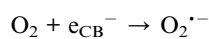
These radicals initiate oxidative degradation by breaking carbon–nitrogen and carbon–carbon bonds in the antibiotic molecules.

Oxygen vacancies as active sites for charge carrier separation:

Oxygen vacancies (OVs) in BFCO play a crucial role in modulating charge carrier dynamics and enhancing photocatalytic efficiency. These vacancies, which arise from the partial removal of lattice oxygen during synthesis or photocatalytic cycling, serve as active sites for pollutant adsorption and electron trapping.

$$BFCO \rightarrow BFCO^* + V_O + \frac{1}{2}O_2$$

here, V_O represents an oxygen vacancy in the lattice, and BFCO* denotes the defect-rich structure. The presence of these vacancies enhances the mobility of charge carriers, effectively reducing electron–hole recombination. Oxygen vacancies act as electron-trapping sites, stabilizing the photogenerated electrons and allowing them to participate in redox reactions more efficiently.

$$V_O + e_{CB}^- \rightarrow V_O^{\bullet}$$
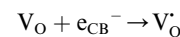
The oxygen-deficient sites also facilitate the adsorption of O_2 molecules, which are then reduced by trapped electrons to generate superoxide radicals ($O_2^{\bullet-}$), a critical species in pollutant degradation.

$$O_2 + V_O^{\bullet} \rightarrow O_2^{\bullet-}$$
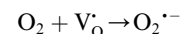
This mechanism significantly boosts ROS formation, accelerating the breakdown of CIP and LFX.

Charge transfer enhancement by mixed-valence states:

BFCO exhibits mixed valence states due to the presence of Fe and Cr in multiple oxidation states, primarily Fe^{3+}/Fe^{2+} and Cr^{3+}/Cr^{2+}. These redox-active centers facilitate rapid interfacial charge transfer, further suppressing electron–hole recombination and improving photocatalytic activity.

Iron redox cycle:

The Fe^{3+}/Fe^{2+} transition provides an efficient electron transport pathway, preventing excess charge accumulation:

$$Fe^{3+} + e_{CB}^- \rightarrow Fe^{2+}$$

$$Fe^{2+} + O_2 \rightarrow Fe^{3+} + O_2^{\bullet-}$$
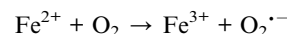
The cyclic reduction and oxidation of Fe ions enhance the generation of superoxide radicals and sustain the degradation process over extended reaction times.

Chromium redox cycle:

Similarly, the Cr^{3+}/Cr^{2+} redox couple contributes to improved charge separation.

3.7.3 Degradation pathways of CIP and LFX. Ring-opening reactions and intermediate formation:

CIP and LFX undergo ring-opening reactions driven by ROS. The superoxide radicals ($O_2^{\bullet-}$) generated from electron transfer in BFCO play a key role in breaking the aromatic and heterocyclic rings of the antibiotic molecules.

$$\text{Hydroxylated CIP/LFX} + O_2^{\bullet-} \rightarrow \text{ring-opened products}$$
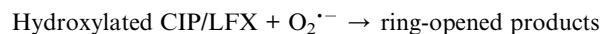
The cleavage of the quinolone ring significantly reduces the antimicrobial activity of these compounds, ensuring that even before complete mineralization, their toxicity in wastewater is substantially lowered. Piperazine ring cleavage leads to the formation of smaller organic acids and amide intermediates.

Stepwise oxidation of organic intermediates:

The fragmented antibiotic molecules undergo further oxidation by superoxide radicals, resulting in the conversion of the intermediates into smaller organic fragments.

$$\text{Ring-opened products} + O_2^{\bullet-} \rightarrow \text{smaller organic fragments}$$

Complete mineralization:

In the final stage, the smaller organic fragments undergo oxidation to produce carbon dioxide (CO_2) and water (H_2O).

$$\text{smaller organic fragments} + O_2^{\bullet-} \rightarrow CO_2 + H_2O$$

This complete mineralization ensures that no toxic organic residues remain in the treated water, making BFCO an environmentally sustainable photocatalyst for wastewater treatment.

4 Conclusions

In conclusion, this study presents the successful synthesis of BiFe$_{0.5}$Cr$_{0.5}$O$_3$ nanocatalysts *via* a sol–gel route, followed by comprehensive characterizations to evaluate their structural integrity, surface morphology, elemental composition, magnetic ordering, and optical properties. Cr substitution led to improved crystallinity, oxygen vacancy formation, and a narrowed bandgap, enhancing visible-light absorption and promoting reactive oxygen species generation. Electrochemical and photoelectrochemical measurements indicated improved charge carrier separation and lower charge transfer resistance, key to boosting photocatalytic activity. Photocatalytic optimization studies identified ideal operational conditions, and under solar irradiation, BiFe$_{0.5}$Cr$_{0.5}$O$_3$ demonstrated highly effective degradation of pharmaceutical pollutants. The material also exhibited favorable reaction kinetics, high apparent quantum yield, and low activation energy, underscoring its efficiency in light-driven catalysis. Reactive species trapping experiments confirmed the involvement of specific oxidative radicals in the degradation process. Reusability tests and post-catalysis characterization revealed excellent structural stability and sustained performance across multiple cycles. Based on the collective findings, a mechanistic pathway for pollutant degradation was proposed. However, further research is needed to assess its performance in real wastewater matrices, its stability under varying conditions, and the potential environmental risks from catalyst leaching. Altogether, this work establishes BiFe$_{0.5}$Cr$_{0.5}$O$_3$ as a robust, efficient, and environmentally benign photocatalyst with significant promise for real-world pharmaceutical wastewater treatment applications.

Data availability

The data supporting this article have been included as part of the ESI.†

Conflicts of interest

There are no conflicts to declare.

Acknowledgements

Notes and references

1 J. Xue, D. Lei, X. Zhao, Y. Hu, S. Yao, K. Lin, Z. Wang and C. Cui, *Chemosphere*, 2022, **291**, 132837.

2 A. Singh, S. G. Pratap and A. Raj, *Environ. Sci. Pollut. Res.*, 2024, **31**, 47505–47529.

3 S. Khan, M. Naushad, M. Govarthanan, J. Iqbal and S. M. Alfadul, *Environ. Res.*, 2022, **207**, 112609.

4 R. Shanmuganathan, M. S. Kadri, T. Mathimani, Q. H. Le and A. Pugazhendhi, *Chemosphere*, 2023, **332**, 138812.

5 S. Hube, M. Eskafi, K. F. Hrafnkelsdóttir, B. Bjarnadóttir, M. Á. Bjarnadóttir, S. Axelsdóttir and B. Wu, *Sci. Total Environ.*, 2020, **710**, 136375.

6 R. Rashid, I. Shafiq, P. Akhter, M. J. Iqbal and M. Hussain, *Environ. Sci. Pollut. Res.*, 2021, **28**, 9050–9066.

7 M. B. Bahrodin, N. S. Zaidi, N. Hussein, M. Sillanpää, D. D. Prasetyo and A. Syafiuddin, *Curr. Pollut. Rep.*, 2021, **7**, 379–391.

8 A. Hussain, R. Kumari, S. G. Sachan and A. Sachan, in *Microbial Ecology of Wastewater Treatment Plants*, Elsevier, 2021, pp. 175–192.

9 C. Zhao, J. Zhou, Y. Yan, L. Yang, G. Xing, H. Li, P. Wu, M. Wang and H. Zheng, *Sci. Total Environ.*, 2021, **765**, 142795.

10 A. Kumar and D. Pal, *J. Environ. Chem. Eng.*, 2018, **6**, 52–58.

11 V. Homem and L. Santos, *J. Environ. Manage.*, 2011, **92**, 2304–2347.

12 B. C. Hodges, E. L. Cates and J.-H. Kim, *Nat. Nanotechnol.*, 2018, **13**, 642–650.

13 Y. Chen, W. Ren, T. Ma, N. Ren, S. Wang and X. Duan, *Environ. Sci. Technol.*, 2024, **58**, 4844–4851.

14 B. Liu, X. Liu, Y. Li, M. Xiao, Z. Chen, S. Wang, H. Wang and X. Wang, *Eco-Environ. Health*, 2024, **3**, 418–424.

15 D. Bahnemann, *Sol. Energy*, 2004, **77**, 445–459.

16 Q. Guo, C. Zhou, Z. Ma and X. Yang, *J. Adv. Mater.*, 2019, **31**, 1901997.

17 A. Mclaren, T. Valdes-Solis, G. Li and S. C. Tsang, *J. Am. Chem. Soc.*, 2009, **131**, 12540–12541.

18 J.-Y. Li, Y.-H. Li, M.-Y. Qi, Q. Lin, Z.-R. Tang and Y.-J. Xu, *ACS Catal.*, 2020, **10**, 6262–6280.

19 J. A. Rengifo-Herrera and C. Pulgarin, *J. Chem. Eng.*, 2023, 146875.

20 A. Baig, M. Siddique and S. Panchal, *Catalysts*, 2025, **15**, 100.

21 X. Zheng, Y. Liu, Y. Yang, Y. Song, P. Deng, J. Li, W. Liu, Y. Shen and X. Tian, *Renewables*, 2023, **1**, 39–56.

22 R. K. Sahu, T. Patodia, S. Juyal, F. S. Gill, B. Prasad and A. Jain, *Catal. Sci. Technol.*, 2025, **15**(4), 988–1002.

23 S. Deng, N. Wang, Y. Zhu and K. Thummavichai, *Catal. Sci. Technol.*, 2024, **14**, 6443–6465.

24 S.-M. Lam, Z.-J. Yong, J.-C. Sin, A. R. Mohamed, H. Zeng, H. Li, H. Lin, L. Huang, H. Huang, L. Xu, et al., *Appl. Surf. Sci.*, 2025, **691**, 162702.

25 S.-M. Lam, J.-C. Sin, H. Zeng, H. Li, H. Lin, L. Huang, J.-W. Lim and K. Dong, *Sep. Purif. Technol.*, 2024, **329**, 125249.

26 J.-C. Sin, S.-M. Lam, H. Zeng, H. Lin, H. Li, L. Huang, S.-J. Liaw, A. R. Mohamed, J.-W. Lim, K. Dong, et al., *Ceram. Int.*, 2024, **50**, 5372–5383.

27 J.-C. Sin, S.-M. Lam, H. Zeng, H. Lin, H. Li, L. Huang, S.-J. Liaw, A. Mohamed and J.-W. Lim, *Mater. Today Sustain.*, 2023, **22**, 100340.

28 S.-M. Lam, J.-C. Sin, M. W. W. Tong, H. Zeng, H. Li, L. Huang, H. Lin and J.-W. Lim, *Chemosphere*, 2023, **344**, 140402.

29 T. Zhou, T. Zhai, H. Shen, J. Wang, R. Min, K. Ma and G. Zhang, *Chemosphere*, 2023, **339**, 139678.

30 C. Ponraj, G. Vinitha and J. Daniel, *Environ. Nanotechnol., Monit. Manage.*, 2017, **7**, 110–120.

31 G. Catalan and J. F. Scott, *Adv. Mater.*, 2009, **21**, 2463–2485.

32 T. Zhao, A. Scholl, F. Zavaliche, K. Lee, M. Barry, A. Doran, M. Cruz, Y. Chu, C. Ederer, N. Spaldin, et al., *Nat. Mater.*, 2006, **5**, 823–829.

33 C. Ederer and N. A. Spaldin, *Phys. Rev. B: Condens. Matter Mater. Phys.*, 2005, **71**, 224103.

34 T. V. Rozario, F. Sharmin, S. Shamim and M. A. Basith, *Ceram. Int.*, 2024, **50**, 3606–3617.

35 R. Zhang, P. Hu, L. Bai, X. Xie, H. Dong, M. Wen, Z. Mu, X. Zhang and F. Wu, *Phys. Chem. Chem. Phys.*, 2022, **24**, 5939–5945.

36 T. Bavani, J. Madhavan, S. Prasad, M. S. AlSalhi and M. J. AlJaafreh, *Environ. Pollut.*, 2021, **269**, 116067.

37 L. Chen, B. Guan, J. Guo, Y. Chen, Z. Ma, J. Chen, S. Yao, C. Zhu, H. Dang, K. Shu, et al., *Catal. Sci. Technol.*, 2023, **13**, 5478–5529.

38 S. Kharbanda, N. Dhanda, A.-C. A. Sun, A. Thakur and P. Thakur, *J. Magn. Magn. Mater.*, 2023, **572**, 170569.

39 Â. Gonçalves, M. Matias, J. A. Salvador and S. Silvestre, *Int. J. Mol. Sci.*, 2024, **25**, 1600.

40 D. Chen, F. Niu, L. Qin, S. Wang, N. Zhang and Y. Huang, *Sol. Energy Mater. Sol. Cells*, 2017, **171**, 24–32.

41 Y. Ma, P. Lv, F. Duan, J. Sheng, S. Lu, H. Zhu, M. Du and M. Chen, *J. Alloys Compd.*, 2020, **834**, 155158.

42 E. Djatoubai, M. S. Khan, S. ul Haq, P. Guo and S. Shen, *Appl. Catal., A*, 2022, **643**, 118737.

43 Z. Nazeer, I. Bibi, F. Majid, S. Kamal, M. I. Arshad, A. Ghafoor, N. Alwadai, A. Ali, A. Nazir and M. Iqbal, *ACS Omega*, 2023, **8**, 24980–24998.

44 S. Irfan, S. Rizwan, Y. Shen, L. Li, Asfandiyar, S. Butt and C.-W. Nan, *Sci. Rep.*, 2017, **7**, 42493.

45 S. Irfan, L. Li, A. S. Saleemi and C.-W. Nan, *J. Mater. Chem. A*, 2017, **5**, 11143–11151.

46 M. Sahni, S. Kumar, S. Chauhan, M. Singh, S. Pandit, P. C. Sati, M. Kumar, A. Kumar and N. Kumar, *Mater. Today: Proc.*, 2022, **49**, 3015–3021.

47 S. Irfan, Y. Shen, S. Rizwan, H.-C. Wang, S. B. Khan and C.-W. Nan, *J. Am. Ceram. Soc.*, 2017, **100**, 31–40.

48 A. Puhan, B. Bhushan, S. Satpathy, S. Meena, A. Nayak and D. Rout, *Appl. Surf. Sci.*, 2019, **493**, 593–604.

49 S. Kumar, F. Ahmed, N. Ahmad, N. M. Shaalan, R. Kumar, A. Alshoaibi, N. Arshi, S. Dalela, M. Albossed, K. H. Chae, et al., *Materials*, 2022, **15**, 4118.

50 Y. Nassereddine, M. Benyoussef, B. Asbani, M. El Marssi and M. Jouiad, *Nanomaterials*, 2023, **14**, 51.

51 M. Tarek, F. Yasmeen and M. A. Basith, *Nanoscale*, 2025, **17**, 6620–6636.

52 M. Tarek, F. Yasmeen and M. A. Basith, *J. Mater. Chem. A*, 2024, **12**, 25475–25490.

53 M. M. Rahman, F. Yasmeen, M. Tarek and M. A. Basith, *J. Alloys Compd.*, 2024, **1010**, 177295.

54 M. Tarek, F. Yasmeen and M. A. Basith, *J. Mater. Chem. A*, 2025, **13**, 499–516.

55 A. Sinha, B. Bhushan, R. Sharma, S. Sen, B. Mandal, S. Meena, P. Bhatt, C. Prajapat, A. Priyam, S. Mishra, et al., *Results Phys.*, 2019, **13**, 102299.

56 A. Sinha, B. Bhushan, D. Rout, R. Sharma, J. Gupta, S. Sen, M. Mukadam, S. Meena and S. Yusuf, *AIP Conf. Proc.*, 2017, **1832**(1), 050088.

57 Y. Wang and X. Zhang, *J. Magn. Magn. Mater.*, 2022, **560**, 169570.

58 J. Li and X. Y. Guan, *Micro Nano Lett.*, 2019, **14**, 1307–1311.

59 C. Himcinschi, F. Drechsler, D. S. Walch, A. Bhatnagar, A. A. Belik and J. Kortus, *Nanomaterials*, 2022, **12**, 1607.

60 S. Shankar, I. Maurya, A. Raj, S. Singh, O. Thakur and M. Jayasimhadri, *Appl. Phys. A*, 2020, **126**, 1–10.

61 F. Zhan, G. Wen, R. Li, C. Feng, Y. Liu, Y. Liu, M. Zhu, Y. Zheng, Y. Zhao and P. La, *Phys. Chem. Chem. Phys.*, 2024, **26**(15), 11182–11207.

62 G. Vinai, A. Khare, D. Rana, E. Di Gennaro, B. Gobaut, R. Moroni, A. Y. Petrov, U. Scotti di Uccio, G. Rossi, F. Miletto Granozio, et al., *APL Mater.*, 2015, **3**, 116107.

63 P. Makuła, M. Pacia and W. Macyk, *J. Phys. Chem. Lett.*, 2018, **9**, 6814–6817.

64 M. A. Adib, F. Sharmin and M. A. Basith, *Nanoscale Adv.*, 2023, **5**, 6194–6209.

65 F. Yasmeen, M. Tarek and M. A. Basith, *ACS Appl. Mater. Interfaces*, 2024, **16**, 47535–47550.

66 M. J. Hosen, M. Tarek, M. D. I. Bhuyan, M. A. Basith and I. M. Syed, *Nanoscale Adv.*, 2025, **7**, 1742–1753.

67 M. Tarek and M. A. Basith, *J. Mater. Chem. C*, 2023, **11**, 16605–16622.

68 A. Islam, M. Tarek, R. Rashid, M. A. A. Bally, F. Ara and M. A. Basith, *Mater. Adv.*, 2025, **6**, 1379–1391.

69 M. Islam, M. Tarek, M. A. Adib and M. A. Basith, *J. Phys. D: Appl. Phys.*, 2024, **57**, 215302.

70 M. S. Ali, S. Das, Y. F. Abed and M. A. Basith, *Phys. Chem. Chem. Phys.*, 2021, **23**, 22184–22198.

71 V. Ramar and K. Balasubramanian, *ACS Appl. Nano Mater.*, 2021, **4**, 5512–5521.

72 M. A. Abbasi, Z. Ali, Z. Qamar, K. Shahzad, H. K. Siddiqui, M. Atif, Z. Ali and W. Khalid, *Ceram. Int.*, 2021, **47**, 14390–14398.

73 H. Maleki, *J. Mater. Sci.: Mater. Electron.*, 2018, **29**, 11862–11869.

74 N. Zhang, D. Chen, F. Niu, S. Wang, L. Qin and Y. Huang, *Sci. Rep.*, 2016, **6**, 26467.

75 J. Hulett, *Q. Rev., Chem. Soc.*, 1964, **18**, 227–242.

76 J. Velázquez, R. Fernández-González, L. Díaz, E. P. Melián, V. Rodríguez and P. Núñez, *J. Alloys Compd.*, 2017, **721**, 405–410.

77 S. Ghosh, K. Chakraborty, T. Pal and S. Ghosh, *Sci. Rep.*, 2023, **13**, 19028.

78 M. J. Muñoz-Batista, A. Kubacka and M. Fernández-García, *Catal. Sci. Technol.*, 2014, **4**, 2006–2015.

79 J. Barrio, D. Mateo, J. Albero, H. García and M. Shalom, *Adv. Energy Mater.*, 2019, **9**, 1902738.

80 A. Trenczek-Zajac, M. Synowiec, K. Zakrzewska, K. Zazakowny, K. Kowalski, A. Dziedzic and M. Radecka, *ACS Appl. Mater. Interfaces*, 2022, **14**, 38255–38269.

© 2025 The Author(s). Published by the Royal Society of Chemistry